

Article

Estimating a Non-Linear Economic Model for a Small-Scale Pyrolysis Unit

Alok Dhaundiyal ^{1,*} , András Máté Betovics ² and Laszlo Toth ³¹ Centre for Energy Research, 1121 Budapest, Hungary² Doctoral School of Technical Sciences, Hungarian University of Agriculture and Life Sciences, 2100 Godollo, Hungary³ Institute of Technology, Hungarian University of Agriculture and Life Sciences, 2100 Godollo, Hungary

* Correspondence: dhaundiyal.alok@ek.hun-ren.hu

Abstract: This article used control theory to derive a non-linear exergoeconomic model for a bench-scale pyrolysis unit. A combination of an autoregressive model with an exogenous input model was involved to investigate the energy system. The economic prospects of the unit were also examined by assigning the cost to the exergy content of the energy stream. The analysis covered the detailed evaluation of the design and performance of an updraft system. Thermally processed pine waste was used as a feedstock for the reactor. The developed model fits well with the validation data extracted through the experimental findings. The exergy cost flow rate of processed pine waste was estimated to be $0.027 \text{ €}/\text{s}^{-1}$. The exergoeconomic factor was the highest for pyrolysis oil and charcoal generated as the end products of the thermal decomposition of processed pine waste.

Keywords: gas dynamics; control engineering; reactor; pellet; exergy costing



Academic Editor: Franco Berruti

Received: 24 November 2024

Revised: 5 January 2025

Accepted: 19 January 2025

Published: 20 January 2025

Citation: Dhaundiyal, A.; Betovics, A.M.; Toth, L. Estimating a Non-Linear Economic Model for a Small-Scale Pyrolysis Unit. *Energies* **2025**, *18*, 445. <https://doi.org/10.3390/en18020445>

Copyright: © 2025 by the authors. Licensee MDPI, Basel, Switzerland. This article is an open access article distributed under the terms and conditions of the Creative Commons Attribution (CC BY) license (<https://creativecommons.org/licenses/by/4.0/>).

1. Introduction

Modern bioenergy is the genesis of newly developed infrastructure in industry and academia that is powered via a renewable energy mix or relies on co-fire-based technologies. The share of the same is around 55% of the net renewable energy source and about 6% of the global supply chain. The rapid advancement of modern bioenergy is due to the recent paradigm shift in emission policies. The net-zero emission by 2050 demands a swift replacement of conventional fuels by bio-based fuels. From 2010 to 2021, a rise of 7% was noticed in the utilization of modern bioenergy. Additional endeavors have been sought to gain momentum in deploying modern bioenergy technologies with the common line of action, i.e., Net Zero 2050. It was predicted that the installation of modern bioenergy would be enhanced by 10% by 2030 without any detrimental impact on society and its local environment [1]. Bioenergy, an asymptote to a zero-emission fuel, is one of the main columns used to decarbonize current energy sources. Since bioenergy is quite flexible with the conversion technologies, it can be used in residential complexes and industrial plants as a source of heat energy. Some positive outcome related to biofuel is predicted in small and heavy industries. A jump of 7% is predicted in Biojet kerosene by 2030, which is nearly zero in 2021. Liquid biofuel consumption is expected to increase from 2.10 Mboe to over 8 Mboe during 2021–2030, primarily for land transportation purposes. A hike of around 54.54% in bioenergy could be materialized by 2030 in cement, pulp, paper, and other small-scale industries. A steep rise in electrical energy generation through bioenergy from 750 TW·h (about 2.5% of total demand) to 1350 TW·h (about 3.5% of total demand) will be visible by 2030. The negative emission is another benchmark of bioenergy that is also

forecasted to play a pivotal role in achieving carbon neutrality. From 2 Mt of CO₂ in 2021 to around 250 Mt of CO₂ in 2030 is assumed to be controlled through BECCS (bioenergy with carbon capture and storage) [2]. Globally, the United States, Canada, Brazil, Indonesia, and India constitute 80% of global expansion in biofuel utilization, since these nations have holistic policy packages that promote sustainable growth. In Europe, stumbling transport fuel demand has nearly impeded volume growth despite having stringent state-level policies. Internationally, a spike of 5.4% during 2022–2027 has been noticed in the biofuel consumption [1,2]. To materialize the objectives of meeting net zero-emission, additional momentum can be granted by involving biofuel production from waste resources. The International Energy Agency proclaimed that 100 EJ of sustainable biomass can be derived from woody residues, organic wastes, forest plantation, and short-rotation woody crops planted on marginal land. These agriculture and forest resources also provided 50 EJ of energy through liquid biofuel production. It is predicted that biofuel demand may reach up to 14 EJ by 2040, whereas gasification and pyrolysis technologies can transform these available feedstocks at a production cost of less than 50% as compared to conventional technologies [3]. Aligning with similar conversion technologies, some challenges and the qualitative impact of feedstock on the process are covered by a literature review based on pyrolysis and gasification.

Kersten et al. (2005) discussed the two-dimensional and first-dimensional models of Di Blasi and Bamford for biomass pyrolysis, respectively. It was concluded that the size of biomass particles influences the conversion time. For small particles (≤ 3 mm) with a lower external heat transfer coefficient (α), the influence of α on the conversion time is perceivable. However, the particles with higher aspect ratios had a similar conversion time for both 1D and 2D models. It was also commented that the external heat transfer coefficient has minimal impact on the product yields at typical fast pyrolysis temperatures [4–6]. Bridgewater (2012) concluded the advantages of fast pyrolysis while dealing with storage and transportation issues. However, there is an economic disadvantage in it being more costly than fossil-based energy and other non-technical issues while attempting to bargain in the energy market [7]. Lak et al. (2023) proposed an innovative multigeneration system that is used for district heating and cooling, and the production of bioethanol, biogas, and electricity. Around 15 biomass sources were used to operate the system. Through the process simulation using FORTRAN and Aspen Plus, it was found that the Cotton stem had the highest CO₂ emission (195.30 kg/MW·h), whereas switchgrass emitted the lowest (147.00 kg/MW·h). Similarly, the exergy efficiency of the plant for rice straw was the highest (68.30%). On the contrary, it was noticed to be the lowest for rick husk [8]. Shan et al. (2022) proposed a biomass-driven thermophotovoltaic (TPV) technology to exhibit better utilization of the energy as compared to the direct solar TPV. It was reported that the percentage loss of exergy was highest during the combustion of biomass, which amounted to 40%. The increasing fraction of moisture in biomass caused the TPV efficiency to drop by more than 3%. It was also proposed that the extended area of TPV and modification to the regenerator might curtail the exergy loss of flue gas and could improve TPV efficiency by more than 10% [9]. Fakayode et al. (2021) examined the exergy of ultrasound-assisted deep eutectic solvent-pretreated watermelon rind (WMR). Later, the processed biomass underwent co-pyrolysis with coal. The exergy of watermelon rind was increased by 34.01% after the pretreatment process [10]. Sezer and Ozveren (2021) proposed an artificial neural network (ANN) to examine the exergy of the syngas. The maximum exergy predicted for olive cake is 17.47 MJ·kg⁻¹, whereas it is the least for coffee husk (12.48 MJ·kg⁻¹) [11]. Tosun et al. (2023) applied the five exergetic indices to examine a Biomass-integrated Gasification Combine Cycle (BIGCC) coupled with Liquid Metal Magnetohydrodynamics (LMMHD). Based on the analysis, it was concluded that the BIGCC had an average exergy efficiency

of 49% under daily ambient temperature for a year at different air-to-fuel ratio (AFR) [12]. He et al. (2022) proposed a genetic algorithm to investigate a biomass-driven heat and power cogeneration system. For municipal solid waste, the highest exergy was 41.36% and the CO₂ emission was curtailed by 0.90 t/MW·h. The simulated solution showed that the exergy of the same biomass was increased by 1.62% during the optimization process. Integration of the Stirling engine with the stand-alone system had the highest exergy and the lowest carbon dioxide [13]. Yoder et al. (2011) discussed the economic pros and cons of having a joint production of biochar and bio-oil. The primary controlling factor was the heating rate of pyrolysis and based on the same, and it was reported that slow pyrolysis was more favorable for biochar production than fast pyrolysis. Relatively speaking, the economic vantage point would count on the cost of two outputs, i.e., biochar and bio-oil. It was claimed that slow pyrolysis would be beneficial from an economic standpoint since the cost of biochar rises relatively to the price of bio-oil [14]. Gill et al. (2021) performed a series of experiments on hard- and softwood pellets and wooden chips. It was explained that the elemental composition had an insignificant influence on product yield and quality. The quality of bio-oil was claimed to be affected by O/C ratio [15]. However, several parameters impact product yield and they were not comprehensively covered in the study. Wang et al. (2005) conducted experiments on cylindrical particles of pine, beech, bamboo, and demolition wood and it was concluded that a temperature of 450–500 °C would be favorable to obtain the maximum bio-oil yield with the least water content. It was also stated that the orientation of particles in the fluid bed did not affect much the conversion time and bio yield while undergoing thermal decomposition at 500 °C; however, the water content in the produced bio-oil yield was remarkably augmented for the particles larger than 3 mm [16]. Amutio et al. (2012) performed experiments on pinewood using a conical sprouted bed reactor. It was reported that the bio-oil yield was maximum at the thermal decomposition temperature of 500 °C. It was also claimed that the char with a high surface area is suitable for active char production if the pyrolysis is conducted at 600 °C [17]. Thoharudin et al. (2023) reported that the exergy and energy of the non-condensable gas would increase with the temperature rise, whereas those of char would be dropped. The exergy and energy of the bio-oil were claimed to be maximum at a pyrolysis temperature of 500 °C. The higher feeding rate enhanced the energy and exergy efficiencies of the fluidized bed reactor [18]. However, they did not discuss the temperature distribution of the bed while discussing the exergy of the system. However, some other methodologies can be incorporated to simulate the behavior of fluidized beds [19–21], but they have not been addressed much in thermal system design. Chen et al. (2020) combined the Computational Fluid Dynamics/Discrete Element Method (CFD-DEM) and a multi-step reaction scheme to analyze a fluidized bed reactor. It was noticed that the increase in temperature from 500 to 700 °C resulted in a rise in light gas yield from 17% to 25%, whereas char yield dropped by 36.36%. It was also claimed that the particle size is relatively undermined by the operating temperature range while determining the yield of products of pyrolysis [22]. Wang et al. (2016) adopted a conventional approach to determine the energy and exergy of a two-stage fixed-bed pyrolysis reactor. It was reported that the rate of change in exergy and energy was maximum at 1000 °C. The carbon monoxide gas had the highest contribution while evaluating the exergy and energy for an operating range of 800–900 °C. Likewise, methane comprised the highest quota in exergy and energy values when the same reactor operated between 1000 °C to 1200 °C. However, the exergy and energy efficiencies of the unreacted carbon and tar dropped with the increasing temperature of the reactor [23]. Nayak and Datta (2022) proposed an entropy-based TOPSIS (Technique for Order Preference by Similarity to an Ideal Solution) multi-criteria decision-making method (MCDM) to rank and select a suitable rice husk (RH) variety among four varieties

of paddy: Badsha-bhog, Lal-swarna, IR-36, and Shankar [24]. Nayak and Datta (2022) attempted to encourage RH as a potential energy feedstock by optimizing paddy variety selection. Thermogravimetry showed that the activation energy of different RHs varied from $96.43 \text{ kJ}\cdot\text{mol}^{-1}$ to $99.37 \text{ kJ}\cdot\text{mol}^{-1}$ for an operating range of $185\text{--}390 \text{ }^\circ\text{C}$ [24]. So, the optimization of feedstock could be an alternative way to assess the exergy of the system. Venugopal et al. (2018) applied a non-stoichiometric equilibrium model based on Gibbs free energy minimization to simulate the gasification of rice husk. They used FACTSAGE version 6.3 to analyze the system. The maximum exergy of the mixture was reported at the equivalence ratio (φ) of 0.25 and $725 \text{ }^\circ\text{C}$. The increase in φ reduced the hydrogen content, whereas the operating temperature was reported to have a reverse effect on hydrogen percentage [25]. Zalazar et al. (2022) performed a macro-scale thermogravimetric analysis of a pellet of pistachio waste. It was reported that the biochar and gas yields dropped by 19.44% and 14.28% with the increasing heating rate, respectively. Conversely, the bio-oil yield was enhanced to 40% for the same range of heating rates [26]. Peters et al. (2014) simulated the fast pyrolysis plant using Aspen Plus. The overall exergetic efficiency of the plant was noticed to be 71.20%, whereas energy degradation was seen in the gas-and-char combustor of the plant. The degree of irreversibility was also recorded to be relatively high in the pyrolysis reactor, the bio-oil recovery section, the dryer, and the mill. The overall plant efficiency was measured to be 73.20% [27]. However, no modelling was performed, and the results relied on the database of the software. Tiara et al. (2019) performed an exergy analysis of an oil palm empty fruit bunch to determine the effectiveness of the pyrolysis reactor during the conversion process. Based on Gibbs free energy, it was estimated the maximum hydrogen percentage would be perceived at the beginning of $355 \text{ }^\circ\text{C}$. The exergy estimation counted on the pyrolytic reaction of the cellulose. It was reported that the maximum exergy efficiency of 96.33% would be obtained at $450 \text{ }^\circ\text{C}$, where 1 mol of cellulose would produce 5 mol of CO, 1 mol of methane, and 3 mol of hydrogen [28]. Wang et al. (2014) proposed an exergy model for a typical coal pyrolysis system with a feeding capacity of $1000 \text{ kg}\cdot\text{h}^{-1}$ for raw lignite. It was reported that the maximum energy loss took place during the drying process of coal and the maximum exergy loss occurred inside the pyrolysis reactor owing to the higher thermal gradient at the first reaction stage. The energy quality factor was proposed to evaluate the grade of pyrolysis products, and it was claimed that the tar had a relatively higher energy grade than that of semi-coke and syngas [29].

Predominately, the methodologies [17,18,23,28] were based on the conventional scheme, which relies on theoretical evidence rather than developing a unique approach to assess the thermal system. Based on the theoretical model proposed by Tsatsaronis (1993) [30], a machine learning technique was used to develop a non-linear economic model that involves temporal variation in the cost associated with the exergy of the system powered by processed pine waste (PPN).

2. Materials and Methods

2.1. Mathematical Modelling of Energy System

A non-linear black-box system identification method, an autoregressive (AR) model with an exogenous input (X) model, was used to evaluate the physical exergy of a laboratory-scale pyrolysis unit. The output exergy of the gas (regressand) was estimated by evaluating regressors. The dynamic value of the regressor relies on the current and past sampling data and the past value of exergy as a part of a chain of causes and effects. In other words, the regressors are mainly the input and output that are related to the latency of the system. All these regressors are the input feeds to the non-linear and linear blocks of the non-linearity estimator. However, it is up to the user end who can decide which subset of regressors would be the input of the non-linear block. The non-linearity estimator block

maps the regressors to the model response variable using the combination of non-linear and linear functions. As compared to the conventional scheme or other non-linear system identification models [31], it provides flexibility to adjust the regressor by the response variable. It is to be noted that it is possible to exclude either linear or non-linear functions whilst estimating the output of the model.

Mathematically:

$$\psi = J^T(f(t) - H) + d + K(M(f(t) - H)) \quad (1)$$

Here, J , H , d , and K are the model parameters. The first and second terms in Equation (1) denote the outputs of the linear function and non-linear function blocks, respectively. M represents the projection or influence matrix to map the vector of response values to the vector of fitted values. The parameter d is a scalar offset. In case $d \neq 0$, the term $J^T(f(t) - H) + d$ represents affine. The block diagram of the non-linear ARX model is shown in Figure 1.

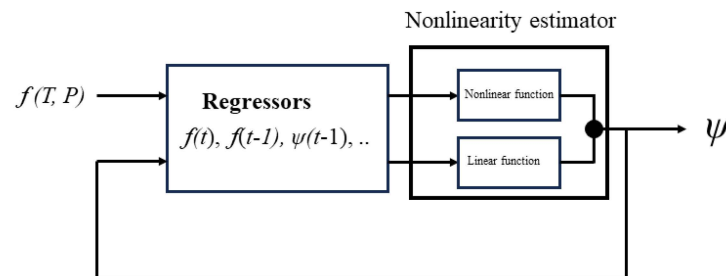


Figure 1. The block diagram of the non-linear ARX model.

It is to be noted a non-linear dynamic system has been considered in this study, which makes it different from a linear dynamic system with static non-linearity owing to saturation and dead zone, as seen in the H–W model [20].

2.2. Exergoeconomics of Pyrolysis Unit

Economics encompasses the exergoeconomics of the small pyrolysis unit, which provides an insight into the costs associated with initial investment, operating cost, and maintenance and fuel cost. Another aspect covered in this analysis was related to exergy costing, which is related to the cost of energy carrier, exergy destruction, and exergy losses.

Disregarding the change in kinetic and potential energy at the inlet and outlet, the energy as well as entropy balance can be estimated using Equations (2) and (3), respectively.

$$\dot{Q} + \dot{W} = \sum_{j=1}^N m_j h_j - \sum_{i=1}^n m_i h_i \quad (2)$$

Here, m_j and m_i are, respectively, the mass streams leaving and entering the system, whereas \dot{Q} and \dot{W} represent the heat transfer and work exchange at arbitrary temperature T between the system and its surroundings. The term h denotes the specific enthalpy associated with the mass streams entering at the inlet, i and leaving at an outlet, j .

Similarly:

$$\frac{\dot{Q}}{T} + \dot{S}_{gen} = \sum_{j=1}^N m_j s_j - \sum_{i=1}^n m_i s_i \quad (3)$$

\dot{S}_{gen} is the entropy generation rate, whereas the term s denotes the specific entropy of the system.

In the same manner, the exergy of the system within its boundary would be equal to the change in the exergy, $\delta\psi^s$, along with its destruction, $\delta\epsilon_D$, which can further be divided

into the exergies associated with heat transfer ($\delta\psi_{\dot{Q}}$), work exchange ($\delta\psi_{\dot{W}}$), and the mass stream m entering and leaving the system [30,32].

$$\delta\psi^s + \delta\varepsilon_D = \delta\psi_Q + \delta\psi_W - p_0 dV + \sum_{i=1}^n \delta\psi_i^s - \sum_{j=1}^N \delta\psi_j^s \quad (4)$$

The additional term, $-p_0 dV$, Denotes the work performed at the moving boundary by or on the surroundings. Here, p_0 and dV are the pressure of the environment and the change in the system volume, respectively.

For the steady state condition, it can be written as

$$\dot{\varepsilon}_D = \dot{\psi}_Q + \dot{\psi}_W + \sum_{i=1}^n \dot{\psi}_i^s - \sum_{j=1}^N \dot{\psi}_j^s \quad (5)$$

Here, $\dot{\varepsilon}_D$ denotes the exergy destruction rate. The terms on the left side of Equation (5), $\dot{\psi}_Q$, $\dot{\psi}_W$, $\dot{\psi}_i^s$, and $\dot{\psi}_j^s$, represent the exergy flow rates associated with heat and work transfer rates and the mass flow rates m_i and m_j at the inlet and outlet of the system, s , respectively. If in this case the system is subdivided into k components, then the summation of energy destruction at each stage can be estimated by using Equation (6).

$$\varepsilon_{D,\text{total}} = \sum_{l=1}^{l=k} \varepsilon_{Dl} \quad (6)$$

In the same manner, the exergy related to the heat transfer Q can be computed through Equation (7):

$$\psi_Q = \left(1 - \frac{T_0}{T}\right) Q \quad (7)$$

The total exergy of the material stream (ψ^T) can be calculated by adding the physical exergy (ψ_{PH}) and chemical exergy (ψ_{CH}).

$$\psi^T = \psi_{PH} + \psi_{CH} \quad (8)$$

Conventionally, the physical exergy of an energy carrier can be defined as the sum of thermal exergy (ψ_{TH}) and mechanical exergy (ψ_{ME}) [30,32].

$$\psi_{PH} \approx \psi_{TH} + \psi_{ME} \quad (9)$$

In other words, physical exergy for an open (control) system for product stream can be given by

$$\psi_{PH} = (b - b_0) - T_0(s - s_0) \quad (10)$$

b , s , and T represent the Keenan function, entropy of the system, and the temperature of the surroundings, respectively.

The chemical exergy of solid fuel or gaseous fuel can be estimated by determining the chemical composition at the reference state T_0 and P_0 .

If the mass ratio of oxygen (O) to carbon (C) is $\frac{O}{C} < 0.667$, and Equation (11) can be used to calculate the chemical exergy of solid fuel [33].

$$\psi_{CH} = (NCV)_0 \left[1.0437 + 0.1882 \left(\frac{H}{C} \right) + 0.0610 \left(\frac{O}{C} \right) + 0.0404 \left(\frac{N}{C} \right) \right] \quad (11)$$

where H and N denote the fraction of hydrogen and nitrogen present in a solid fuel. The term NCV represents the net calorific value of the solid fuel.

For solid fuel with a mass ratio of $2.67 > \frac{O}{C} > 0.667$

$$\psi_{CH} = (NCV)_0 \frac{\left[1.0438 + 0.1882\left(\frac{H}{C}\right) - 0.2509\left\{1 + 0.7256\left(\frac{H}{C}\right)\right\} + 0.0383\left(\frac{N}{C}\right)\right]}{\left(1 - 0.3035\left(\frac{O}{C}\right)\right)} \quad (12)$$

In the case of the gaseous and liquid fuel, Equations (13) and (14) were used.

$$\psi_{CH} = -\Delta h_0 + T_0 \Delta s_0 + RT_0 \left[x_{O_2} \ln\left(\frac{p_{O_2}}{P_0}\right) - \sum x_q \ln\left(\frac{p_q}{P_0}\right) \right] \quad (13)$$

where x_{O_2} is the mole fraction of oxygen and the subscript q represents the components of the products of composition. The change in the enthalpy of formation is denoted by Δh_0 . The symbol p_{O_2} denotes the partial pressure of oxygen and P_0 is the total pressure of the gaseous mixture.

$$\psi_{CH} = (NCV)_0 \left[1.0401 + 0.1728\left(\frac{H}{C}\right) + 0.0432\left(\frac{O}{C}\right) + 0.2169\left(\frac{S}{C}\right) \left\{ 1 - 2.0628\left(\frac{H}{C}\right) \right\} \right] \quad (14)$$

The exergetic efficiency of the system can be estimated by using the ratio of the exergy value of the product (ψ_P) to the exergy value of the fuel (ψ_F).

$$\eta_{II} = \frac{\psi_P}{\psi_F} = \left[1 - \left(\frac{\varepsilon_D + \varepsilon_L}{\psi_F} \right) \right] \quad (15)$$

where ε_L is the exergy loss that occurred owing to the design of the reactor.

The exergy destruction in any of the components (ε_{D_i}) can be correlated to total fuel exergy to the updraft unit, total product exergy to the unit and total exergy destruction in the unit ($\varepsilon_{D,total}$).

$$y_1 = \frac{\varepsilon_{D_i}}{\varepsilon_{D,total}} \quad (16)$$

$$y_2 = \frac{\varepsilon_{D_i}}{\psi_F} \quad (17)$$

$$y_3 = \frac{\varepsilon_{D_i}}{\psi_P} \quad (18)$$

The exergy destruction fractions in the unit to total exergy destruction, the exergy of fuel, and the product exergy to the unit are, respectively, represented by y_1 , y_2 , and y_3 .

In the economic analysis, the total capital cost (ζ) included the monetary values related to the investment (sunk cost), and operating and maintenance costs. This total capital cost can be bifurcated into the capital cost associated with the exergy destruction (related to the component size and its efficiency) (ζ_e) and the cost (ζ_0), which is independent of exergy flowthrough and the exergy destruction across a component.

$$\zeta = \zeta_0 + \zeta_e \quad (19)$$

The assessment of the design and performance of a unit can be performed by knowing the fraction of the total cost drained out of the system in the form of exergy destruction. Therefore, it plays a pivotal role in making the energy system cost-effective since the cost incurred to the end users is based on the fraction of energy that can be utilized to perform a task. Also, it is essential to compare technical alternatives and the economic value of the energy carriers. The concept of exergy costing relies on allocating funds to energy carriers and the wastage of the same in the form of exergy destruction and exergy losses. Hence, it is quite reasonable to estimate exergy cost per exergy unit [34,35]. Another aspect of exergy costing is the relative location of a subsystem within the total plant since charging

for the plant owing to exergy destruction and exergy losses at the uniform cost flow rate per unit (tantamount to average costing per exergy unit of the fuel of the plant) will not be important from the thermodynamic and economic point of view [30]. A fraction of total exergy destruction impacts the output of the plant differently; for example, x MW of exergy destruction in the coal gasifier will not impact the electricity generation as much as the same amount of exergy destruction rate in the low-pressure gas turbine.

2.3. Experimental Set-Up

The experimental task was performed at the premises of the Hungarian University of Agriculture and Life Sciences. The data collection was executed via a 16-channel data acquisition system. K-type thermocouples were used to measure the temperature at four different locations across the reactor. The pressure sensor was retrofitted with the lid to determine the dynamic pressure of the producer gas. Thermogravimetric change in the mass of material was based on a strain gauge measurement system. The sampling frequency for the measurement was 2 Hz. As an interface between the developed system and the transducer, the fifth version of the CATMAN module was considered. An orthographic sketch of the reactor is illustrated in Figure 2. The physical set-up of the unit is depicted in Figure 3. To tackle the heating range, a ceramic-based heating system was manually developed that can withstand more than 1000 °C without any dielectric breakdown. However, safety concern was also given priority and therefore an isolation transformer was provided to prevent the external circuit from failing. The voltage set-up to the heating filament was provided via a variable transformer so that a predetermined bed temperature could be met. The electricity measurement of the heating system was performed using the multifunction analyzer. The generated gas was measured through a portable wood gas analyzer equipped with gas wash bottles, a cotton wool filter, activated charcoal with a cotton wool filter, and a series of activated alumina soaked with potassium permanganate filters. To avoid condensation of tar, the gas was allowed to pass through a condensate trap before the gas analyzer. The sample collection rate was 700 mL per minute for the wood gas analyzer. To measure dust and tar content, 50 mL isopropanol was used. An illustrative diagram of the tar collection unit is shown in Figure 4 [36]. Before initializing the gas measurement, the volumetric rate was measured through a gas meter. The ultimate analysis of pine waste and char content is provided in Table 1 [37]. The information related to the equipment used is provided in Table 2.

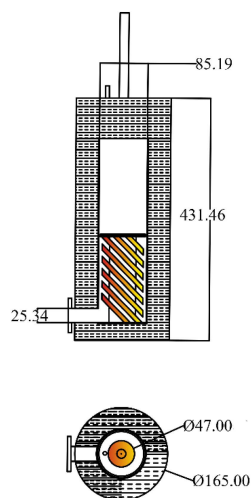


Figure 2. The updraft pyrolysis reactor.

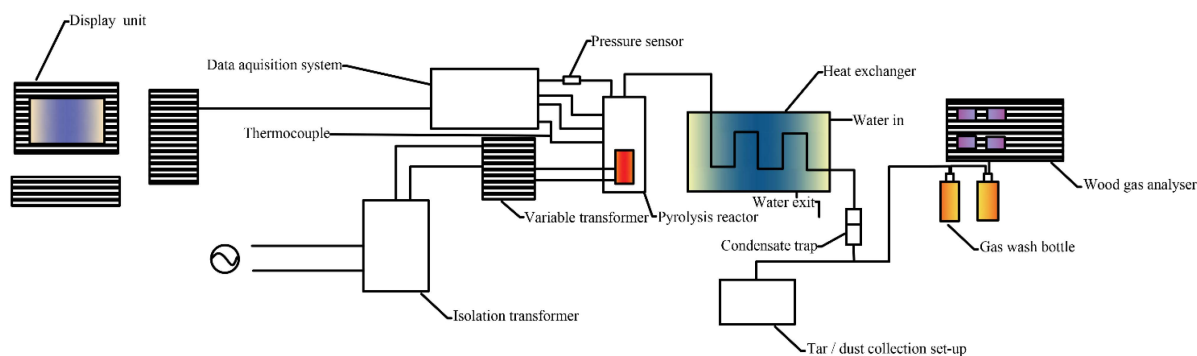


Figure 3. Schematic diagram of the updraft unit.

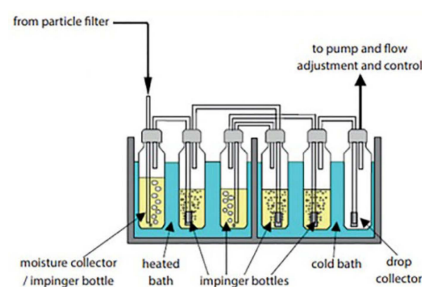


Figure 4. The collection unit for pyrolysis oil [36].

Table 1. The ultimate analysis of pine waste and the char obtained after pyrolysis.

Material Type	C%	H%	N%	O%	S%	Bulk Density ($\text{kg}\cdot\text{m}^{-3}$)	Heating Value ($\text{MJ}\cdot\text{kg}^{-1}$)
PPN	53.40	6.54	0.39	36.79	0.10	730.00	23.44
Char (PPN)	72.65	3.48	1.57	14.17	0.26	-	27

Table 2. The detailed information related to the equipment used for experimental purpose.

Components	Manufacturer	Measuring Range/Capacity/Accuracy
Gas meter	Ganz 2000, Budapest, Hungary	0.04 m^3/h , 0.49 bar
Multifunction analyzer	EMD 90, Contrel Electronica, Lombardy, Italy	Power < 1% Current < 0.5% Voltage < 0.5% Power factor < 1% Measuring range: 30–500 Hz
VY Strain gauge	HBM, Darmstadt, Germany	Nominal resistance: 120–350 Ω
Quantum X data acquisition system (DAQ)	HBM, Darmstadt, Germany	Sampling rate: 250 kHz
Pressure gauge	Huba control AG, Würenlos, Germany	Pressure < 0.5% Measuring range: 0.3–50 mbar
Gas analyzer	VISIT-03H analyzer, Messtechnik EHEIM GmbH, Schwaigern, Germany	Gas volumetric rate: 0.8 L/min Maximum Permissible pressure: 50 mbar

Note: Detailed information related to the economic model/metrology of the unit is provided in Supplementary File S1.

3. Results

3.1. Dynamics of the Energy System

The change in the state properties of the system, temperature, and pressure with time is illustrated in Figure 5a. The variation in reacted mass fraction, α_B , with time is shown in Figure 5b. A maximum pressure rise of 216.66 Pa was noticed at 20.30% of mass reacted during pyrolysis of PPN or at the onset of devolatilization. Similarly, the total pressure

was dropped to 28.77 Pa during the char formation ($\alpha_B = 1$). During the inception stage of water evaporation, the system pressure rose by 434.42% with 0.31% of mass loss. The recorded pressure at the onset of devolatilization was 135 Pa, which was 14.12% higher than that noticed during evaporation. The overall fall in the pressure of the thermodynamic system till the completion of devolatilization was 66.88%, which was further curtailed to 9.5 Pa till the completion of pyrolysis of PPN. The standard deviation in the total pressure measurement across the reactor was ± 55 Pa. The skewness in its distribution pattern about its average value of 55.07 Pa was 0.6. Similarly, the distribution of pressure across the reactor would exhibit the traits of the raised cosine function. The variability in the pressure fluctuation during the decomposition of PPN was seen to be low.

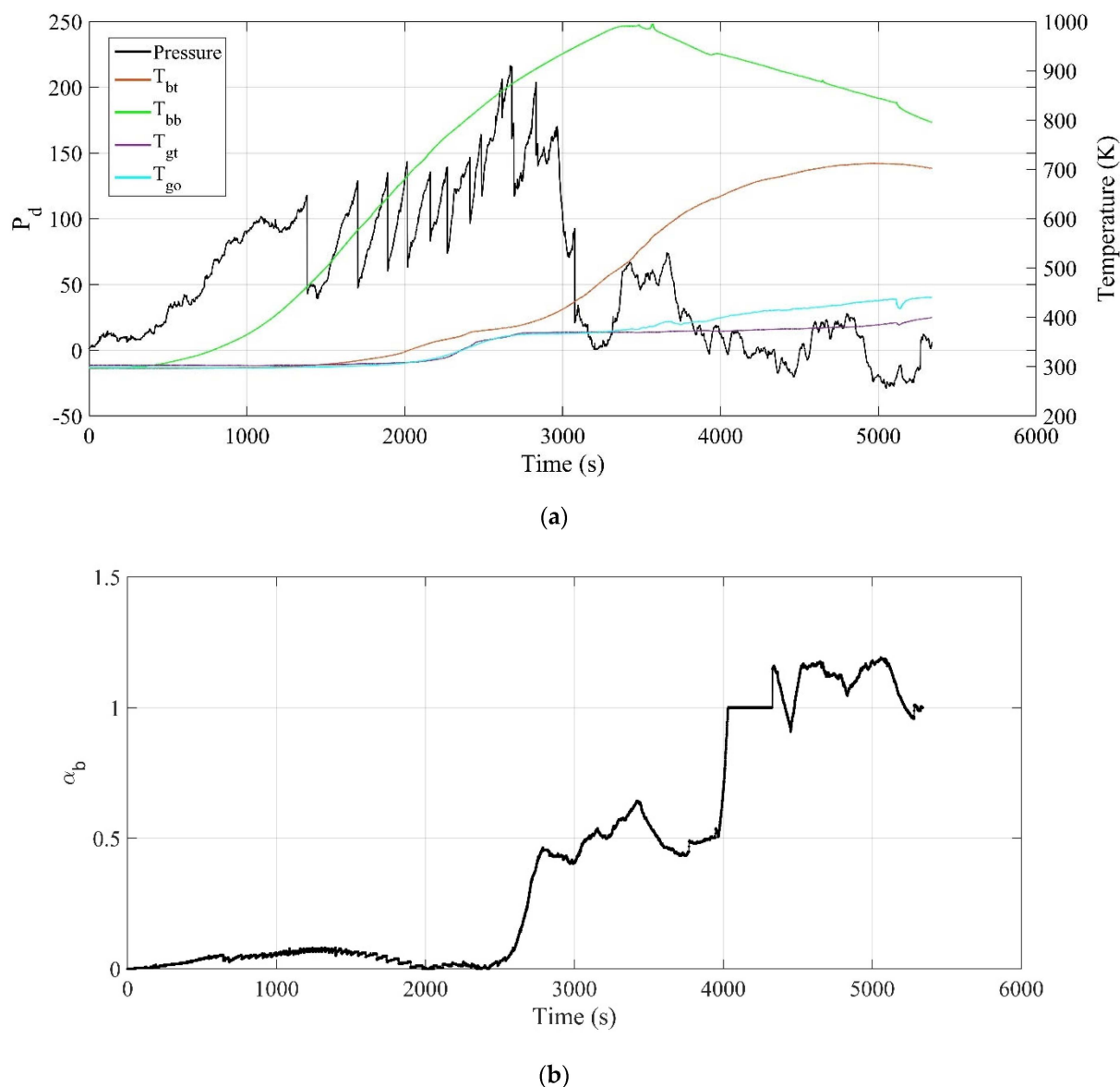


Figure 5. The variation in the state properties (T, P) of the energy system (a) along with reacted mass fraction (b).

The average bed temperature at the bottom surface (T_{bb}) was 708.38 K. The maximum and minimum change in the bed temperature near the bottom surface with time was, respectively, 995.43 K and 298.14 K. The heating rate during the evaporation was noticed to be $7 \text{ K}\cdot\text{min}^{-1}$, which was increased to $12.52 \text{ K}\cdot\text{min}^{-1}$ during the release of the volatile gas. A drop of 50.15% was seen in the heating rate of the reactor during the saturation in the

change of mass of PPN with time. The temperature of the system was seen to be increased by 44.64%. The temperature gradient across the bed was dropped by 45.36% at the end of the devolatilization. The standard deviation in the measurement of T_{bb} was ± 519.90 K. The measured value of T_{bb} is negatively skewed about its mean value. The distribution characteristic of T_{bb} would show a resemblance with the uniform distribution function. Similarly, the average bed surface temperature at (T_{bt}) was 458 K with a standard deviation of ± 437.07 K. The distribution pattern of T_{bt} was noticed to be positively skewed about its mean value with a skewness of 0.48. The change in the surface temperature of the bed after devolatilization was augmented by 92.5% as compared to the onset of it. In the same manner, it was raised by 11.21% during the evaporation of moisture content. Unlike T_{bb} , T_{bt} was enhanced by 8.92% as the saturation in the changing mass of PPN was attained. The average gas temperatures at the surface of the bed (T_{gt}) and at the outlet of the reactor (T_{go}) were, respectively, 399.56 K and 440.16 K. The standard deviation in the gas temperature at the surface of the bed was 288.86 K, whereas it was 292.09 K for T_{go} . A rise of 1.46% in T_{go} was seen at the onset of char formation, which continuously increased with the rate of $20.31 \text{ K}\cdot\text{min}^{-1}$ till the end of the charring process. This happened owing to the exothermic reaction that occurred during the formation of H_2 and CH_4 . The distribution function of T_{gt} was seen to be negatively skewed about its mean value, whereas a positive skewness of 0.22 was in T_{go} . Both T_{gt} and T_{go} would share characteristics of the uniform distribution function with a marginal change in its value over the given period.

The standard uncertainty in the total system pressure during the pyrolysis of PPN was ± 2.94 Pa, whereas the change in the mass of PPN during the thermogravimetric process was ± 0.15 g. Similarly, the uncertainties in the measurement of the bed temperatures at the bottom and top surfaces were, respectively, ± 0.24 K and ± 0.18 K. The gas temperature near the top surface of the packed bed had an uncertainty of ± 0.062 K. Likewise, the observed uncertainty in the gas temperature at the outlet, T_{go} , was ± 0.064 K. The uncertainty associated with the measurement of water temperature in the heat exchanger (HE) (T_w) was ± 0.06 K. The power requirement during the pyrolysis of PPN (P) imparted an uncertainty of ± 1.55 W. The standard uncertainty measured during the experimental work is provided in Table 3.

Table 3. The standard uncertainty in the measurement.

Material	T_{bb} (K)	T_{bt} (K)	P_d (Pa)	T_{gt} (K)	T_{go} (K)	P (W)	T_w (K)	m (g)
PPN	± 0.24	± 0.18	± 2.94	± 0.062	± 0.064	± 1.55	± 0.06	± 0.15 g

3.2. Exergy Analysis

The average value of physical exergy provided for the thermal decomposition of PPN was $81.38 \text{ MJ}\cdot\text{kg}^{-1}$. The maximum exergetic efficiency (η_{II}) reported for the PPN was 68.82%, whereas the average value was estimated to be 46.46%. The exergy destruction fraction (y_1) for PPN was 0.88. As compared to the fuel (y_2) and product exergies (y_3), it was, respectively, 0.08 and 0.16 for PPN. The exergy loss (ϵ_I) to the environment during thermal decomposition of PPN was 45.89 of the total exergy of PPN. In the same way, the exergy destruction (ϵ_D) held a 7.64% share of the total exergy of PPN. The product material streams comprised gas generation and charcoal and oil production. Based on the exergy analysis, the exergy efficiency of gas production was 71.90%. The remaining 24.14% of the total physical exergy of gas was lost due to the irreversibility in the system, while 3.94% sank into the environment during the transmission. The generation of charcoal accompanied 12.80% of exergy lost to the environment through the reactor and removal from the reactor, whereas 22.19% of the physical exergy was lost due to exergy destruction. The percentage fraction of exergy destruction during the char formation was 1% of the total exergy destruction of

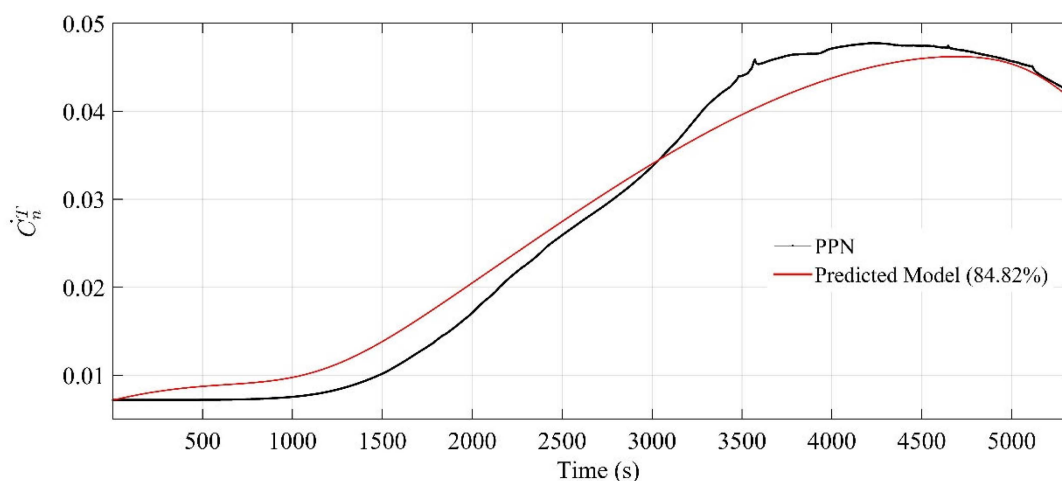
the system, whereas it was 0.87% and 0.47% for oil and gas, respectively. In the case of the heating system, the exergy destruction was increased to 6% of the total exergy destruction. The lowest exergy destruction was estimated for heat exchanger and pump, which was 0.068% and 0.05% of the total exergy destruction, respectively. The exergy loss during the thermal decomposition of PPN was 98.14% of the total exergy loss of the unit, followed by the heating system and reactor. The lowest exergy loss fraction was observed during the operation of the auxiliary pump, which was 0.002% of the total exergy loss in the unit. The indirect heating to the reactor was provided through a heating filament with exergetic efficiency of 13.04%. Similarly, the heat exchanger and the pump were able to utilize 78.08% and 87.81% of the total input exergy to the system, respectively. Detailed information related to the computed physical and chemical exergies is provided in Table 4.

Table 4. The exergy content of components and material streams.

Component/Material Stream	ψ_{PH}	ψ_{CH}	η_{II}	ε_D	ε_L	y_1	y_2	y_3
Heater	1.61 MJ·kg ⁻¹	00	13.04%	0.63 MJ·kg ⁻¹	0.77 MJ·kg ⁻¹	0.06	5.74 × 10 ⁻³	0.01
Reactor	0.55 MJ·kg ⁻¹	00	49.10%	0.21 MJ·kg ⁻¹	0.07 MJ·kg ⁻¹	0.02	1.91 × 10 ⁻³	4.11 × 10 ⁻⁰³
Heat exchanger	65.80 kJ·kg ⁻¹	00	78.08%	7.11 kJ·kg ⁻¹	7.31 kJ·kg ⁻¹	6.86 × 10 ⁻⁴	6.47 × 10 ⁻⁵	1.39 × 10 ⁻⁴
Pump	58.99 kJ·kg ⁻¹	00	87.81%	6.12 kJ·kg ⁻¹	1.07 kJ·kg ⁻¹	5.91 × 10 ⁻⁴	5.57 × 10 ⁻⁵	1.20 × 10 ⁻⁴
PPN	81.38 MJ·kg ⁻¹	28.37 MJ·kg ⁻¹	46.46%	8.39 MJ·kg ⁻¹	50.37 MJ·kg ⁻¹	0.88	0.08	0.16
Gas	0.21 MJ·kg ⁻¹	0.15 MJ·kg ⁻¹	71.90%	50.70 kJ·kg ⁻¹	8.29 kJ·kg ⁻¹	4.76 × 10 ⁻³	4.61 × 10 ⁻⁴	9.94 × 10 ⁻⁴
Charcoal	0.68 MJ·kg ⁻¹	33.21 MJ·kg ⁻¹	65%	150.91 kJ·kg ⁻¹	87.05 kJ·kg ⁻¹	0.01	1.37 × 10 ⁻³	2.95 × 10 ⁻³
Oil	0.23 MJ·kg ⁻¹	16.51 MJ·kg ⁻¹	72.73%	93.42 kJ·kg ⁻¹	15.28 kJ·kg ⁻¹	8.78 × 10 ⁻³	8.51 × 10 ⁻⁴	1.83 × 10 ⁻³
Total	84.78 MJ·kg ⁻¹	79.61 MJ·kg ⁻¹	-	9.53 MJ·kg ⁻¹	51.32 MJ·kg ⁻¹	-	-	-

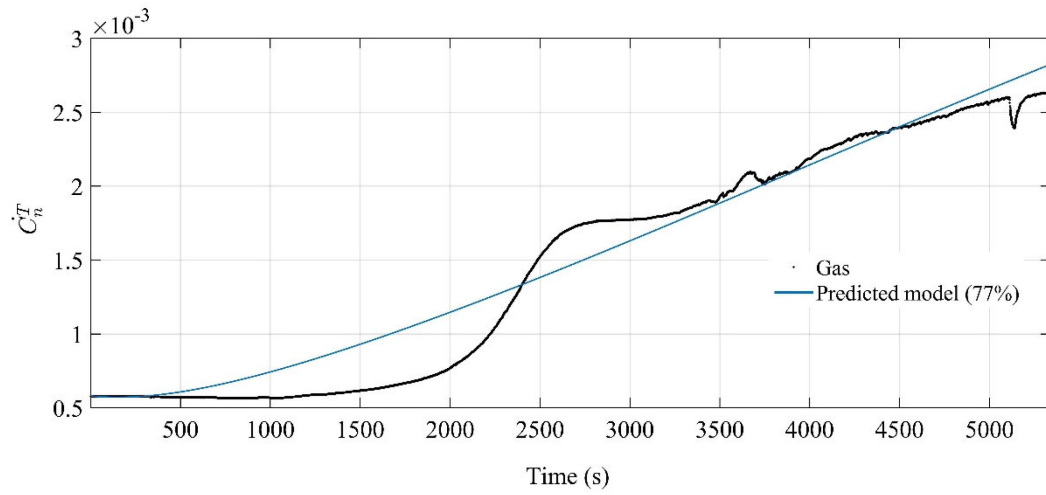
3.3. Exergoeconomics of the Energy System

The ARX model was adopted to develop the exergy cost model for different material streams, which was fitted against the validation data in Figure 6a–e. Detailed information related to the different exergy costs is provided in Tables 5 and 6. The comparison of validation data of the relative change in product and fuel cost (I) with predicted model flow is illustrated in Figure 7a–e.

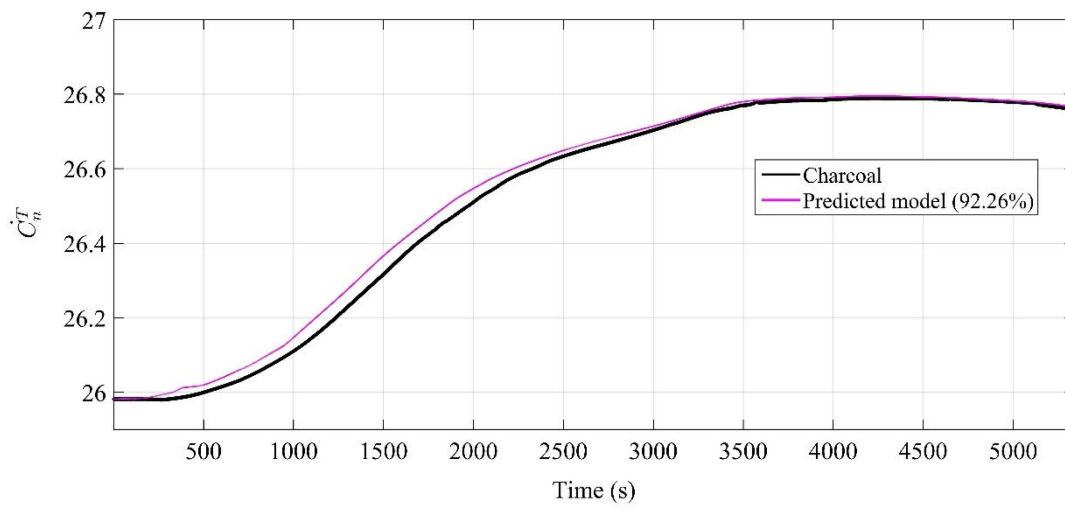


(a)

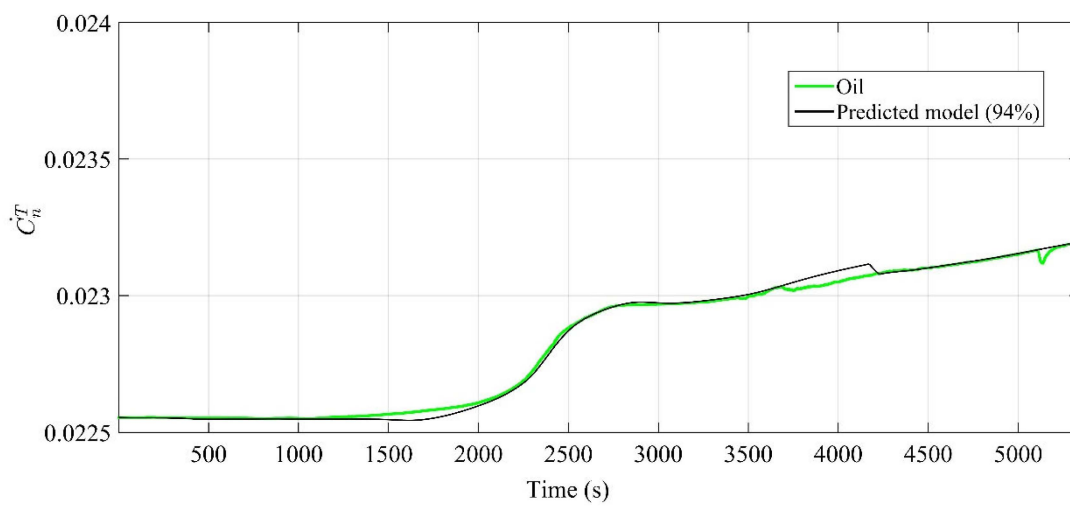
Figure 6. Cont.



(b)

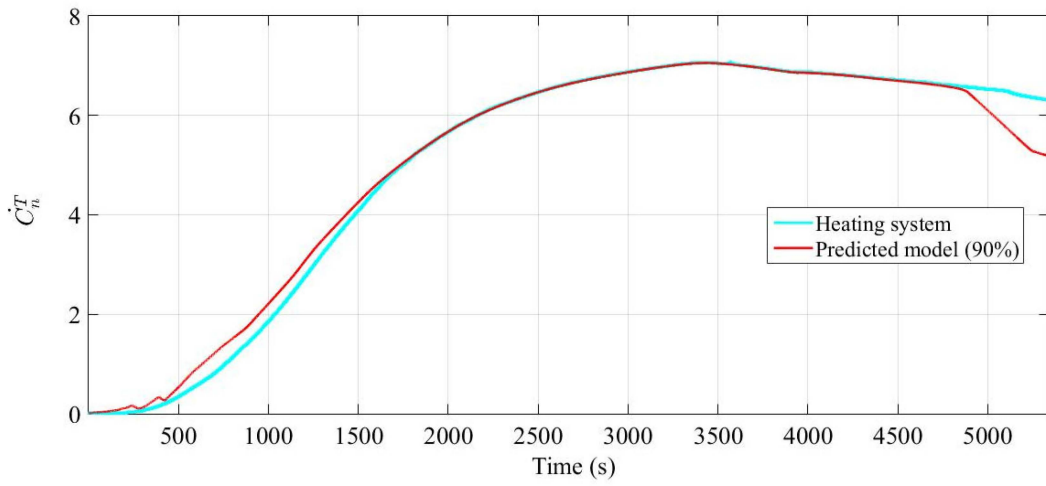


(c)



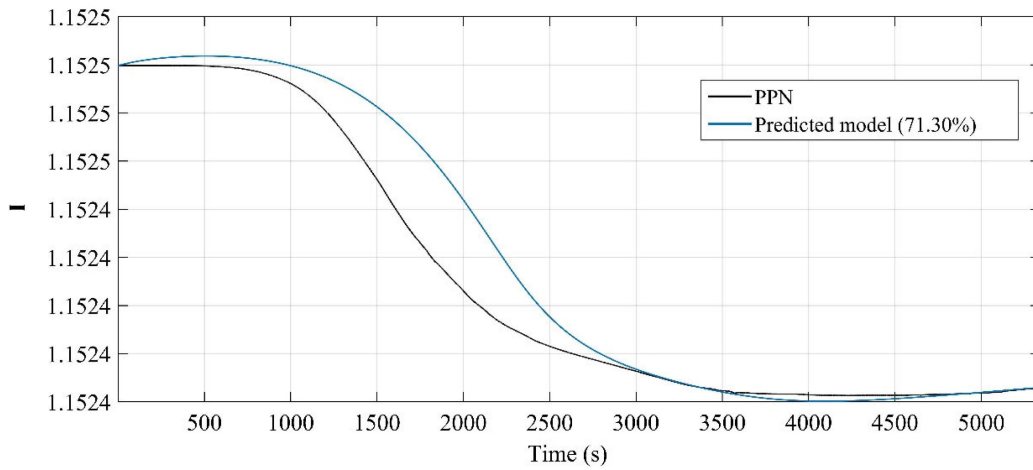
(d)

Figure 6. Cont.

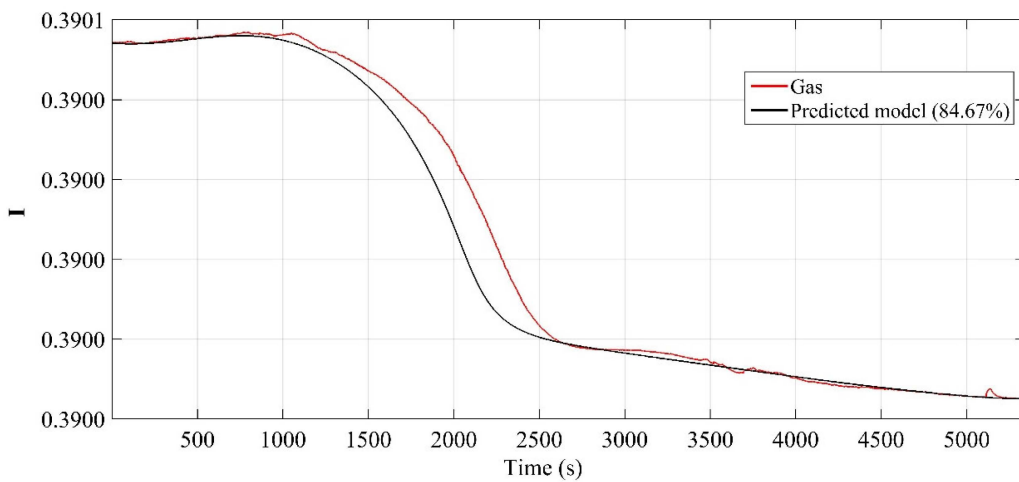


(e)

Figure 6. The variation in the exergy cost rate (\dot{C}_n^T) of the material stream with time ((a)—PPN; (b)—gas; (c)—charcoal; (d)—oil; (e)—heater).

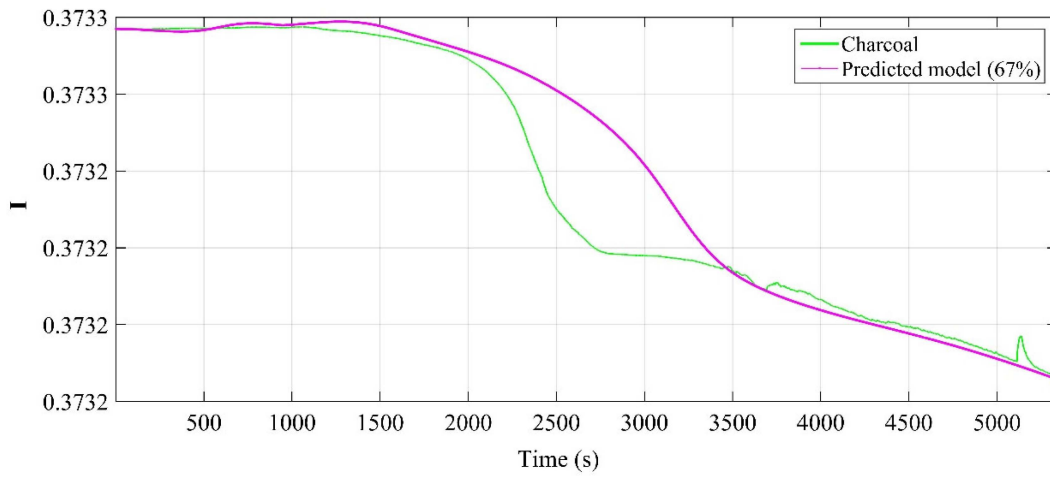


(a)

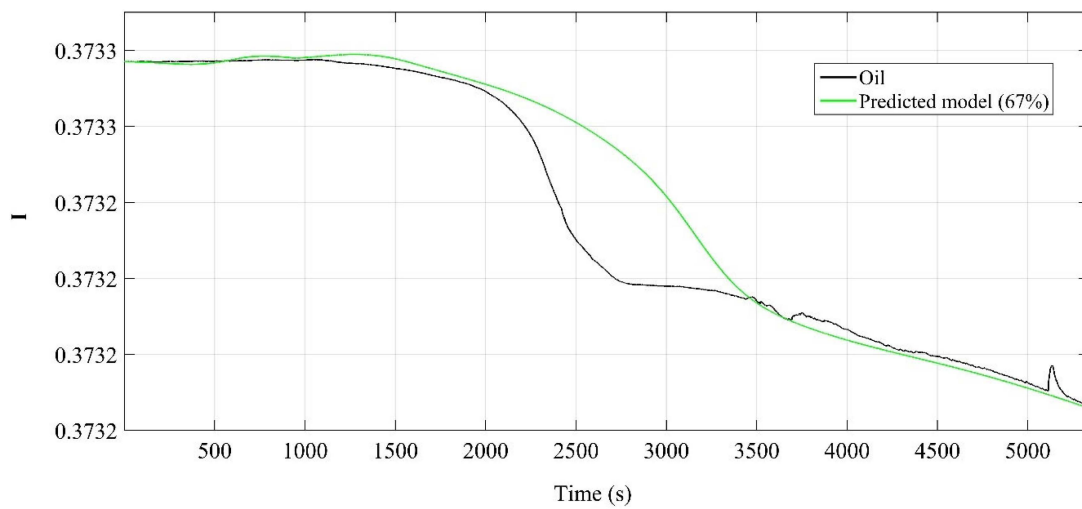


(b)

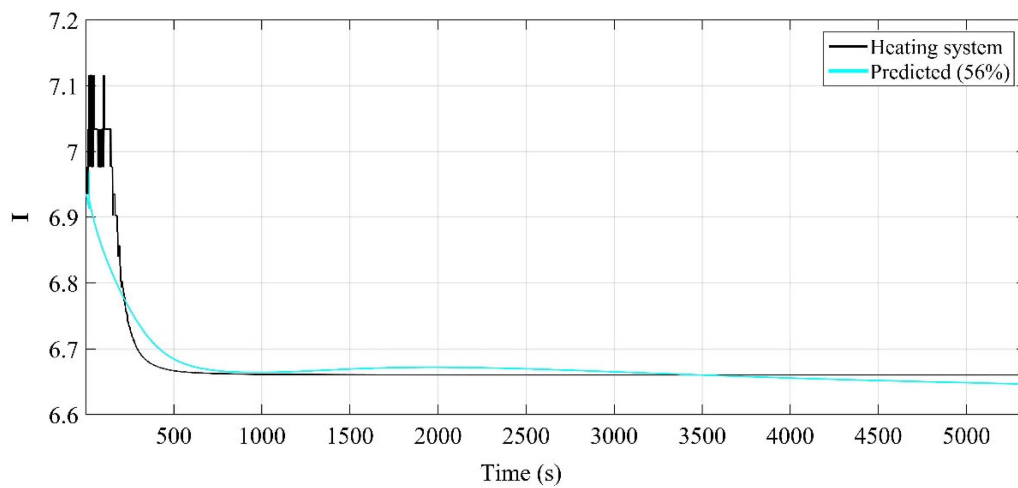
Figure 7. Cont.



(c)



(d)



(e)

Figure 7. The change in the average relative change in fuel and product cost (I) with time ((a)—PPN, (b)—Gas, (c)—Charcoal, (d)—Oil, (e)—Heating system).

Table 5. The average exergy cost associated with components and material streams.

Component/Material Stream	\dot{C}_n^T	\dot{C}_j^T	$\dot{C}_{L,l}^T$	O_l	I
PPN	$0.027 \text{ €}\cdot\text{s}^{-1}$	$0.24 \text{ €}\cdot\text{s}^{-1}$	$8.60 \times 10^{-3} \text{ €}\cdot\text{s}^{-1}$	0.22	1.15
Gas	$0.0017 \text{ €}\cdot\text{s}^{-1}$	$0.04 \text{ €}\cdot\text{s}^{-1}$	$8.70 \times 10^{-5} \text{ €}\cdot\text{s}^{-1}$	0.95	0.39
Charcoal	$26.51 \text{ €}\cdot\text{s}^{-1}$	$35.22 \text{ €}\cdot\text{s}^{-1}$	$0.06 \text{ €}\cdot\text{s}^{-1}$	0.99	0.53
Oil	$0.022 \text{ €}\cdot\text{s}^{-1}$	$8.68 \text{ €}\cdot\text{s}^{-1}$	$0.01 \text{ €}\cdot\text{s}^{-1}$	0.99	0.37
Heater	$5.01 \text{ €}\cdot\text{s}^{-1}$	$13.79 \text{ €}\cdot\text{s}^{-1}$	$4.70 \text{ €}\cdot\text{s}^{-1}$	0.01	6.67

Table 6. Comparison between the predicted model and the validation data.

Component/Material Stream	\dot{C}_n^T			RMSE	I			RMSE
	Validation Data	Predicted Model	Non-Linearity		Validation Data	Predicted Model	Non-Linearity	
PPN	$0.027 \text{ €}\cdot\text{s}^{-1}$	$0.025 \text{ €}\cdot\text{s}^{-1}$	Sigmoidnet	8.07×10^{-5}	1.15	1.16	Sigmoidnet	$\pm 3.87 \times 10^{-4}$
Gas	$0.0017 \text{ €}\cdot\text{s}^{-1}$	$0.0016 \text{ €}\cdot\text{s}^{-1}$	Sigmoidnet	$\pm 6.32 \times 10^{-6}$	0.39	0.37	Sigmoidnet	± 0.01
Charcoal	$26.51 \text{ €}\cdot\text{s}^{-1}$	$20.37 \text{ €}\cdot\text{s}^{-1}$	Wavenet	± 0.26	0.53	0.52	Wavenet	$\pm 5.80 \times 10^{-2}$
Oil	$0.022 \text{ €}\cdot\text{s}^{-1}$	$0.025 \text{ €}\cdot\text{s}^{-1}$	Wavenet	$\pm 2.63 \times 10^{-4}$	0.37	0.37	Wavenet	$\pm 4 \times 10^{-3}$
Heater	$5.01 \text{ €}\cdot\text{s}^{-1}$	$5.02 \text{ €}\cdot\text{s}^{-1}$	Wavenet	$\pm 3.87 \times 10^{-4}$	6.67	6.64	Sigmoidnet	± 0.06

Based on the exergy cost flow rate modelling, it was noticed that the derived value of \dot{C}_n^T for gas generation was $0.0016 \text{ €}\cdot\text{s}^{-1}$ with an RMSE of $\pm 6.32 \times 10^{-6}$, which was 5.88% lower than the validated value of \dot{C}_n^T . The predicted value of I for the gas was 0.37, which dropped by 5.12% as compared to the validated value of I . The RMSE associated with the I model was ± 0.01 . The estimated value of O_l for gas generation was 0.95. The total exergy cost rate estimated for the gas generation (\dot{C}_j^T) was $0.04 \text{ €}\cdot\text{s}^{-1}$ with $\dot{C}_{L,l}^T$ of $8.70 \times 10^{-5} \text{ €}\cdot\text{s}^{-1}$. The percentage fit of model obtained for \dot{C}_n^T was 77%, whereas this fit was increased to 84.67% while predicting the value of I .

The associated average exergy cost rate (\dot{C}_n^T) with the charcoal generation was $26.51 \text{ €}\cdot\text{s}^{-1}$. The maximum and minimum exergy cost rate (\dot{C}_n^T) for the charcoal production were, respectively, $26.78 \text{ €}\cdot\text{s}^{-1}$ and $25.97 \text{ €}\cdot\text{s}^{-1}$. The average predicted value related to charcoal was 23.16% lower than the validation data. The root mean square error (RMSE) computed for the charcoal exergy cost rate model was ± 0.26 . The maximum and minimum values predicted through the Charcoal exergy cost rate model were, respectively, $26.22 \text{ €}\cdot\text{s}^{-1}$ and $25 \text{ €}\cdot\text{s}^{-1}$. The total exergy cost estimated for the charcoal production (\dot{C}_j^T) was $35.22 \text{ €}\cdot\text{s}^{-1}$ with the exergoeconomic factor (O_l) of 0.22. The average relative change in charcoal and PPN cost (I) was 0.53, whereas the derived value of I by the predicted model was 0.52, which was underpredicted by 1.88%. The non-linearity of wave network function provided the fit of 92.26% with the validation data of charcoal for \dot{C}_n^T . The cost flow rate related to the exergy loss ($\dot{C}_{L,l}^T$) was noticed to be $0.06 \text{ €}\cdot\text{s}^{-1}$ for the charcoal generation.

Similarly, the average value of \dot{C}_n^T for the oil production was $0.022 \text{ €}\cdot\text{s}^{-1}$ and the average value obtained by the model was $0.025 \text{ €}\cdot\text{s}^{-1}$ (13.63% over predicted) with the RMSE of $\pm 2.63 \times 10^{-4}$. The value of O_l estimated for the oil was 0.99 with a 37% relative change in I , whereas the solution derived for I by the model was the same. The RMSE associated with the I model for the oil production was ± 0.004 . The value of \dot{C}_j^T for the oil production was $0.04 \text{ €}\cdot\text{s}^{-1}$, whereas the value of $\dot{C}_{L,l}^T$ was $0.01 \text{ €}\cdot\text{s}^{-1}$ for the oil production. The percentage fit of model data with the validation data of \dot{C}_n^T and I was, respectively, 94% and 67%.

The exergy cost flow rate \dot{C}_n^T appended with the PPN was $0.027 \text{ €}\cdot\text{s}^{-1}$; with the average relative change in its value before processing, it (I) was 1.15. The value of \dot{C}_n^T predicted by the derived model was $0.025 \text{ €}\cdot\text{s}^{-1}$ with the RMSE value of $\pm 8.07 \times 10^{-5}$, whereas I model forecasted 1.16 as the average change in the PPN cost after processing it. The RMSE obtained for the I model was $\pm 3.87 \times 10^{-4}$. The percentage fit of models obtained for \dot{C}_n^T and I was, respectively, 84.82% and 74.30%. The obtained value of \dot{C}_j^T for PPN was $0.24 \text{ €}\cdot\text{s}^{-1}$, whereas the cost drained out of the system with the rate of $8.60 \times 10^{-3} \text{ €}\cdot\text{s}^{-1}$.

The heating system powered via a variable transformer incurred an exergy flow rate of $5.01 \text{ €}\cdot\text{s}^{-1}$, whereas the cost related to exergy loss ($C_{L,I}^T$) in the heating unit was $4.70 \text{ €}\cdot\text{s}^{-1}$. The value of I obtained through the model for the heating unit was 6.64, which was 0.44% lower than the validation data. Likewise, the \dot{C}_n^T model provided $5.02 \text{ €}\cdot\text{s}^{-1}$ as the cost flow rate imparted to the total physical exergy of the heating system.

The fitness percentages of \dot{C}_j^T model and I model for the heating unit with the validation data were 90% and 56%, respectively. The RMSE related to \dot{C}_j^T model was $\pm 3.87 \times 10^{-4}$. On the other hand, it was ± 0.06 for the I model estimated for the heating unit.

The number of output regressors (k) and input regressors (l) along with the delay between the input and output (m) and the prediction error in the final prediction error is tabulated in Table 7. The smaller the prediction error, the better the model. Based on the generated solution, the exergy cost models for oil production, gas generation, and PPN provided relatively a good fit with the validation data as compared to models obtained for the charcoal and heating unit. Similarly, the I model derived through the ARX scheme was in good agreement with the validation data for charcoal, oil, and PPN as compared to the heating unit. Based on the analysis work, the derived solution provided good consensus with the theoretical model [30].

Table 7. The detail of model input parameters and Akaike's final prediction error.

Material Stream	Regressors \dot{C}_n^T			Regressors I			Akaike's Final Prediction Error	Akaike's Final Prediction Error
	k	l	m	k	l	m	\dot{C}_n^T	I
PPN	3	3	4	2	2	3	6.63×10^{-12}	1.17×10^{-17}
Gas	2	2	2	2	2	4	6.02×10^{-13}	6.04×10^{-16}
Charcoal	2	2	4	2	2	4	1.45×10^{-09}	8.37×10^{-20}
Oil	2	2	4	6	5	4	2.68×10^{-14}	5.98×10^{-16}
Heater	2	2	1	2	3	3	1.56×10^{-7}	3.46×10^{-5}

4. Conclusions

A thermodynamic system was examined using the exergy cost model, and for the same, a non-linear model was proposed. Based on the exergy distribution and exergoeconomic analysis, the salient points are enumerated as follows:

1. A drastic rise in the pressure was noticed during the dehydration phase of PPN with a corresponding rise in temperature by 50.90%. At the onset of devolatilization, the system pressure rose by 27.80% with a 45% conversion of the PPN during the reaction. The char formation began with a 33.16% fall in pressure and a 5.46% increase in the temperature of the bed. The exergy destruction in a particular component/material stream to the total exergy destruction, the exergy of fuel, and the exergy of the product was noticed to be maximum for PPN, followed by the heating system and the reactor. The maximum exergetic efficiency (η_{II}) estimated based on the component was maximum for the ancillary pump and heat exchanger, followed by maximum

exergy conversion during extraction of pyrolysis oil and scavenging of producer gas from the system.

2. The exergy cost model predominately followed the non-linearity in the form of the sigmoidal and wave network functions. The exergy cost associated with charcoal (C_n^T) reported by the proposed model was $20.37 \text{ €}\cdot\text{s}^{-1}$, an underprediction of the validation data by a margin of 23.38%. Similarly, the exergy cost rate to the pyrolysis oil was overpredicted by a percentage fraction of 13.63%. The overprediction in the change in the relative change in the cost of PPN (I) was 0.86%. Comparatively, the relative cost predicted by the ARX showed a good consensus with the validation for all the material streams. The lowest RMSE (6.32×10^{-6}) was appended with the exergy cost model of the gas, whereas the maximum RMSE was seen in the model associated with charcoal production. In the same way, the best-fitted model with the validation data (I) was related to PPN and oil generation.

Supplementary Materials: The following supporting information can be downloaded at: <https://www.mdpi.com/article/10.3390/en18020445/s1>.

Author Contributions: A.D., Supervision, Validation, Conceptualization, Investigation, Software, Resources, Writing, Formal Analysis, Data Curation, Writing—Review and Editing; L.T., Supervision, Project Administration, Data Curation, Writing—Review and Editing, Resources, Funding Acquisition; A.M.B., Data Curation, Resources. All authors have read and agreed to the published version of the manuscript.

Funding: This research received no external funding.

Data Availability Statement: The original contributions presented in the study are included in the article.

Conflicts of Interest: The authors declare no conflict of interest.

References

1. IEA. *Bioenergy*; IEA: Paris, France, 2022. Available online: <https://www.iea.org/reports/bioenergy> (accessed on 1 May 2024).
2. IEA. *Bioenergy Power Generation*; IEA: Paris, France, 2021. Available online: <https://www.iea.org/reports/bioenergy-power-generation> (accessed on 1 May 2024).
3. IEA. *Is the Biofuel Industry Approaching a Feedstock Crunch?* IEA: Paris, France, 2022. Available online: <https://www.iea.org/reports/is-the-biofuel-industry-approaching-a-feedstock-crunch> (accessed on 1 May 2024).
4. Kersten, S.R.A.; Wang, X.; Prins, W.; van Swaaij, W.P.M. Biomass Pyrolysis in a Fluidized Bed Reactor. Part 1: Literature Review and Model Simulations. *Ind. Eng. Chem. Res.* **2005**, *44*, 8773–8785. [[CrossRef](#)]
5. Di Blasi, C. A Transient, Two-Dimensional Model of Biomass Pyrolysis. *Dev. Thermochem. Biomass Convers.* **1997**, *2*, 147–160. [[CrossRef](#)]
6. Bamford, C.H.; Crank, J.; Malan, D.H. The combustion of wood. Part I. *Math. Proc. Camb. Philos. Soc.* **1946**, *42*, 166–182. [[CrossRef](#)]
7. Bridgwater, A.V. Review of fast pyrolysis of biomass and product upgrading. *Biomass Bioenergy* **2012**, *38*, 68–94. [[CrossRef](#)]
8. Lak Kamari, M.; Maleki, A.; Daneshpour, R.; Rosen, M.A.; Pourfayaz, F.; Alhuyi Nazari, M. Exergy, energy and environmental evaluation of a biomass-assisted integrated plant for multigeneration fed by various biomass sources. *Energy* **2023**, *263*, 125649. [[CrossRef](#)]
9. Shan, S.; Huang, H.; Chen, B.; Wu, H.; Zhou, Z. Performance analysis of biomass driven thermophotovoltaic system from energy and exergy perspectives. *Therm. Sci. Eng. Prog.* **2022**, *33*, 101351. [[CrossRef](#)]
10. Fakayode, O.A.; Wang, Z.; Wahia, H.; Mustapha, A.T.; Zhou, C.; Ma, H. Higher heating value, exergy, pyrolysis kinetics and thermodynamic analysis of ultrasound-assisted deep eutectic solvent pretreated watermelon rind biomass. *Bioresour. Technol.* **2021**, *332*, 125040. [[CrossRef](#)]
11. Sezer, S.; Özveren, U. Investigation of syngas exergy value and hydrogen concentration in syngas from biomass gasification in a bubbling fluidized bed gasifier by using machine learning. *Int. J. Hydrogen Energy* **2021**, *46*, 20377–20396. [[CrossRef](#)]
12. Tosun, D.C.; Açıklalp, E.; Caglar, B.; Altuntas, O.; Hepbasli, A. Proposal of novel exergy-based sustainability indices and case study for a biomass gasification combine cycle integrated with liquid metal magnetohydrodynamics. *Process Saf. Environ. Prot.* **2023**, *174*, 328–339. [[CrossRef](#)]

13. He, F.; Liu, X.; Wang, M.; Zhou, S.; Heydarian, D. Energy, exergy, exergoeconomic, and environmental analyses and multi-objective optimization of a biomass-to-energy integrated thermal power plant. *Alex. Eng. J.* **2022**, *61*, 5629–5648. [[CrossRef](#)]
14. Yoder, J.; Galinato, S.; Granatstein, D.; Garcia-Pérez, M. The economic tradeoff between biochar and bio-oil production via pyrolysis. *Biomass Bioenergy* **2011**, *35*, 1851–1862. [[CrossRef](#)]
15. Gill, M.; Kurian, V.; Kumar, A.; Stenzel, F.; Hornung, A.; Gupta, R. Thermo-catalytic reforming of alberta-based biomass feedstock to produce biofuels. *Biomass Bioenergy* **2021**, *152*, 106203. [[CrossRef](#)]
16. Wang, X.; Kersten, S.R.A.; Prins, W.; van Swaaij, W.P.M. Biomass Pyrolysis in a Fluidized Bed Reactor. Part 2: Experimental Validation of Model Results. *Ind. Eng. Chem. Res.* **2005**, *44*, 8786–8795. [[CrossRef](#)]
17. Amutio, M.; Lopez, G.; Artetxe, M.; Elordi, G.; Olazar, M.; Bilbao, J. Influence of temperature on biomass pyrolysis in a conical spouted bed reactor. *Resour. Conserv. Recycl.* **2012**, *59*, 23–31. [[CrossRef](#)]
18. Thoharudin Hsiau, S.-S.; Chen, Y.-S.; Yang, S. Design optimization of fluidized bed pyrolysis for energy and exergy analysis using a simplified comprehensive multistep kinetic model. *Energy* **2023**, *276*, 127615. [[CrossRef](#)]
19. Dhaundiyal, A. Thermo-Statistical Investigation of the Solar Air Collector Using Least Angle Regression. *Energies* **2023**, *16*, 2461. [[CrossRef](#)]
20. Dhaundiyal, A. Exergy Analysis of a Passive Thermal System Using Hammerstein–Wiener Estimation. *J. Energy Resour. Technol.* **2023**, *145*, 121301. [[CrossRef](#)]
21. Dhaundiyal, A.; Bercesi, G.; Toth, L. Investigation of a vertical closed-loop geothermal system for heating an educational building. *Energy Sci. Eng.* **2022**, *11*, 482–501. [[CrossRef](#)]
22. Chen, T.; Ku, X.; Lin, J.; Ström, H. CFD-DEM Simulation of Biomass Pyrolysis in Fluidized-Bed Reactor with a Multistep Kinetic Scheme. *Energies* **2020**, *13*, 5358. [[CrossRef](#)]
23. Wang, X.; Lv, W.; Guo, L.; Zhai, M.; Dong, P.; Qi, G. Energy and exergy analysis of rice husk high-temperature pyrolysis. *Int. J. Hydrogen Energy* **2016**, *41*, 21121–21130. [[CrossRef](#)]
24. Nayak, P.P.; Datta, A.K. An entropy-based TOPSIS approach for selecting the best suitable rice husk for potential energy applications: Pyrolysis kinetics and characterization of rice husk and rice husk ash. *Biomass Convers. Biorefinery* **2022**. [[CrossRef](#)]
25. Venugopal, D.; Thangavelu, L.; Elumalai, N. Energy, exergy and sustainability analysis of rice husk air gasification process. *Therm. Sci.* **2018**, *23*, 549–560. [[CrossRef](#)]
26. Zalazar-Garcia, D.; Fernandez, A.; Cavaliere, L.; Deng, Y.; Soria, J.; Rodriguez, R.; Mazza, G. Slow pyrolysis of pistachio-waste pellets: Combined phenomenological modeling with environmental, exergetic, and energetic analysis (3-E). *Biomass Convers. Biorefinery* **2022**. [[CrossRef](#)]
27. Peters, J.F.; Petrakopoulou, F.; Dufour, J. Exergetic analysis of a fast pyrolysis process for bio-oil production. *Fuel Process. Technol.* **2014**, *119*, 245–255. [[CrossRef](#)]
28. Tiara, E.S.; Susanto Ginting, A.; Setiawan, R.P.; Joelianingsih; Tambunan, A.H. Exergy Analysis on Pyrolysis Process of Oil Palm Empty Fruit Bunch. *IOP Conf. Ser. Mater. Sci. Eng.* **2019**, *557*, 012058. [[CrossRef](#)]
29. Wang, K.; Sun, R.F.; Zhang, G.P. Energy Efficiency Assessment and Exergy Analysis for Lignite Pyrolysis Process System. *Adv. Mater. Res.* **2014**, *953–954*, 1184–1188. [[CrossRef](#)]
30. Tsatsaronis, G. Thermo-economic analysis and optimization of energy systems. *Prog. Energy Combust. Sci.* **1993**, *19*, 227–257. [[CrossRef](#)]
31. Dhaundiyal, A.; Toth, L. Developing a thermodynamic model for the circulating air using an opaque system. *Energy Sci. Eng.* **2023**, *11*, 3790–3806. [[CrossRef](#)]
32. Bejan, A.; Tsatsaronis, G.; Moran, M. *Thermal Design and Optimization*; Wiley: New York, NY, USA, 1996.
33. Kotas, T.J. *The Exergy Method of Thermal Plant Analysis*; Paragon Publishing: Trowbridge, UK, 1985. [[CrossRef](#)]
34. Tsatsaronis, G. Energy economics and management in industry. In Proceedings of the European Conference I, Algarve, Portugal, 1 August 1984; p. 151.
35. Gaggioli, R.A. (Ed.) *Efficiency and Costing*; ACS Symposium Series; American Chemical Society: Washington, DC, USA, 1983. [[CrossRef](#)]
36. Dhaundiyal, A.; Tewari, P.C. Performance evaluation of throatless gasifier using pine needles as a feedstock for power generation. *Acta Technol. Agric.* **2016**, *19*, 10–18. [[CrossRef](#)]
37. Dhaundiyal, A.; Atsu, D.; Toth, L. Physico-chemical assessment of torrefied Eurasian pinecones. *Biotechnol. Biofuels* **2020**, *13*, 199. [[CrossRef](#)]

Disclaimer/Publisher’s Note: The statements, opinions and data contained in all publications are solely those of the individual author(s) and contributor(s) and not of MDPI and/or the editor(s). MDPI and/or the editor(s) disclaim responsibility for any injury to people or property resulting from any ideas, methods, instructions or products referred to in the content.